An illustrated comparison of processing methods for phase MRI and QSM: removal of background field contributions from sources outside the region of interest

Ferdinand Schweser, Simon Daniel Robinson, Ludovic De Rochefort, Wei Li, Kristian Bredies

HHS Public Access

Author manuscript

NMR Biomed. Author manuscript; available in PMC 2018 April 01.

Published in final edited form as:

NMR Biomed. 2017 April ; 30(4): . doi:10.1002/nbm.3604.

An illustrated comparison of processing methods for phase MRI and QSM: Removal of background field contributions from sources outside the region of interest

Ferdinand Schweser[*],

Department of Neurology, Buffalo Neuroimaging Analysis Center, University at Buffalo, The State University of New York – Jacobs School of Medicine and Biomedical Sciences, Buffalo, NY, USA. University at Buffalo, The State University of New York – MRI Molecular and Translational Imaging Center, Buffalo, NY, USA

Simon Robinson,

Medical University of Vienna – Department of Biomedical Imaging and Image-Guided Therapy, Vienna, Austria

Ludovic de Rochefort,

Centre de Résonance Magnétique Biologique et Médicale (CRMBM), UMR 7339, CNRS, Aix-Marseille Université, France

Wei Li, and

University Texas Health Science Center at San Antonio Research Imaging Institute, San Antonio, TX, USA

Kristian Bredies

University of Graz – Institute for Mathematics and Scientific Computing, Graz, Austria

Abstract

The elimination of so-called background fields is an essential step in phase MRI and quantitative susceptibility mapping (QSM). Background fields, which are caused by sources outside the region of interest (ROI), are often one to two orders of magnitude stronger than tissue-related field variations from within the ROI, hampering quantitative interpretation of field maps. This paper reviews the current literature on background elimination algorithms for QSM and provides insights into similarities and differences between the many algorithms proposed. We discuss the basic theoretical foundations and derive fundamental limitations of background field elimination.

Keywords

QSM; susceptibility mapping; phase imaging; phase processing; review; background field removal

[*]Correspondence to: Ferdinand Schweser, University at Buffalo, The State University of New York – Jacobs School of Medicine and Biomedical Sciences, Department of Neurology, Buffalo Neuroimaging Analysis Center, Buffalo, NY, USA. schweser@buffalo.edu.

Sponsors: none

INTRODUCTION

Magnetic field perturbations generally extend throughout all space and are not restricted to the location of their origin. As a result, the measured magnetic field in a certain region of interest (ROI) generally contains contributions both from sources located inside and sources located outside the ROI (Fig. 1) [1, 2]. Due to the proportionality of magnetic field and Larmor frequency [3], the magnetic field can be easily mapped with, e.g., multi-echo gradient echo sequences [4, 5, 6]. We refer to these mapping techniques as field-mapping MRI in the following.

In field-mapping MRI, the field contributions that are not generated by the sources inside the ROI are usually referred to as *background* contributions. They generally originate from a variety of sources, e.g. inhomogeneity of the static main magnetic field, macroscopic currents[1] (e.g. in the MRI shim coils), or magnetic susceptibility variations outside the ROI [2]. Usually, the strongest contributor to the background field is perturbations caused by the high susceptibility difference between air and tissue of approximately 9 parts per million (ppm). The outside surface of the human body represents such a susceptibility interface, but air-tissue interfaces also exist inside the body, for example in the sinus cavities and the lung. The susceptibility of biological tissue (e.g. the brain) depends on its biochemical composition but usually varies only in the sub-ppm range. Hence, background fields are often one to two orders of magnitude stronger than tissue-related field variations from within the ROI and typically dominate the measured field [7, 8, 9].

The purpose of the *background field removal* step in QSM is to eliminate these superimposed fields to avoid a degrading effect on the calculated susceptibility maps [2]. In this review article we discuss the fundamental physical and mathematical foundations of background field removal, review background removal algorithms and conclude with remarks on practical aspects of background elimination and a quantitative comparison of the different methods. We emphasize theoretical aspects of background field elimination rather than numerical implementation, which is generally covered in the respective original publications. We think this approach allows a deeper understanding of the basics and limitations of background field elimination. Along these lines, we have decided to classify the algorithms based on underlying assumptions – the type of mathematical problem solved and the solution obtained. Compared to other classification schemes employed in the literature that are often more oriented toward aspects of the numerical implementation [9, 8, 1], this classification may appear counterintuitive in parts, but it provides additional insights into similarities and differences of the many algorithms proposed. We begin the review with theoretical foundations of background field removal, including central definitions, introduce and discuss the different classes of algorithms and practical considerations of the ROI definition, and close with a quantitative comparison of the different algorithms in a numerical model. Table 1 provides a comparative overview of the different techniques discussed.

[1]We distinguish here between microscopic currents flowing on the atomic and molecular length scale and macroscopic currents flowing over a macroscopic length. Microscopic currents, such as electron orbital motion, are related to magnetic susceptibility via the generation of microscopic dipoles in an externally applied magnetic field [1].

PHYSICAL AND MATHEMATICAL FOUNDATIONS

Definition of the background field

Traditionally, the term *background field* has been used as a synonym for *external field*, which is defined as the field inhomogeneity generated by sources located outside the ROI, whereas *internal fields* are field inhomogeneities caused by sources located inside the ROI, illustrated in Fig. 1. Internal and background field inhomogeneities may be understood as material-related *demagnetization* fields of (induced) dipole moments [1, 8, 9, 10] that add to the externally applied strong main magnetic field, which is usually considered *homogeneous* (e.g. 3 or 7 Tesla). In practice, the main magnetic field has small inhomogeneities due to magnet geometrical imperfections partially corrected for by the shim coils. The associated static effects similarly contribute to the background field. Because we focus on susceptibility-induced fields, the main magnetic field will be considered as homogeneous in the present review without loss of generality. Indeed, a formal handling of its contribution would only require adding a (harmonic; see below) background contribution to the field mapped inside the MRI bore, which is handled by the methods presented.

In QSM, the ROI is usually the region in which the susceptibility distribution is to be determined. This region can be identical to the signal-yielding part of the object within the field of view, but often only a sub-region of this region is chosen to simplify computations or the improve susceptibility estimation. In the case of a brain examination, the ROI usually includes all brain tissues, but excludes other signal-yielding tissues, such as parts of the skull, the eyes and the neck.

In a first-order approximation, internal and external fields can be considered as being independent from one another allowing the expression of the measured *total field H* (again, describing only demagnetization fields here, without loss of generality) as $H = H_{\text{int}} + H_{\text{ext}}$, where H_{int} and H_{ext} are the internal and the external fields that are traditionally assumed to be generated by susceptibility distributions inside and outside the ROI, respectively [11]. This first-order approximation is warranted for susceptibility values of materials considered as “MR-compatible” (few ppm) [12] because demagnetization fields associated with such materials are five to six orders of magnitude weaker than the inducing externally applied magnetic field [1, 10, 7, 9, 8]. Consequently, second-order interaction effects of demagnetization fields with one another are five to six orders of magnitude smaller than the demagnetization fields itself.

However, the *traditional* definition of internal and background fields through the physical location of the generating susceptibility distributions is ambiguous because the susceptibility values underlying H_{int} *outside* and H_{ext} *inside* of the ROI can to some degree be varied without changing the total field, H (see Appendix A.1). For example, if the susceptibility within the ROI is approximately −9 ppm (e.g. brain tissue) and the susceptibility value is set to a constant – zero, say – outside the ROI, the corresponding internal field will show field inhomogeneities due to the relatively large susceptibility difference between the inside and the outside of the ROI. If, on the other hand, the susceptibility value outside the ROI is set to −9 ppm, field inhomogeneities will be minimized. Related to this internal field extraction problem, QSM generally provides only reference-less susceptibility *difference* maps. In the

majority of QSM studies, the susceptibility values are referenced to the average susceptibility value in the brain.

A resolution to the ambiguity of the internal field definition is offered by defining internal and external fields via the gradient of the susceptibility distribution, which is supported by the fact that only spatial *changes* (gradients) of magnetic susceptibility generate magnetic field perturbations. Internal and external fields can then be defined via a constant zero gradient outside and inside the ROI, respectively. This definition requires introducing a third field component that is caused by the susceptibility change on the boundary of the ROI, which in the following description is referred to as the *boundary field,* H_{bnd} *:* $H = H_{int} + H_{ext} + H_{bnd}$, where the underlying susceptibility (gradient) distribution is split accordingly, $\nabla\chi = \nabla\chi_{int} + \nabla\chi_{ext} + \nabla\chi_{bnd}$, with $\nabla\chi_{int} = 0$ outside the ROI and on its boundary, $\nabla\chi_{ext} = 0$ inside the ROI and on its boundary, and $\nabla\chi_{bnd} = 0$ outside and inside the ROI, but not necessarily on the boundary (∇ is the 3D gradient operator). With this definition, internal and external fields have genuine contributions only from inside and outside the ROI, respectively, but not from the boundary; resulting in a unique definition of internal, external, and boundary fields. The boundary field is non-zero if there is a step-change in susceptibility at the boundary (Fig. 2).

In a discretized setting, we further define a *boundary region* of one voxel inside and outside the ROI boundary which contains the sources of the boundary field (see Fig. 1, enlargement). This boundary region is of practical relevance because the ROI boundary is generally located in regions where the susceptibility distribution changes perpendicular to the boundary, e.g. due to cortical convolutions, pial veins, and the transition between brain tissue and cerebrospinal fluid. Furthermore, most background elimination techniques produce incorrect internal field values or do not at all produce internal field values in this boundary region (see below). However, since the goal of background field elimination is the extraction of the internal field, we will refer to the sum of external and boundary fields as the *background field* ($H_{bkg} = H_{ext} + H_{bnd}$) in the remainder of the review, if not explicitly otherwise stated. However, it should be noted that this redefinition is arbitrary and background elimination algorithms may lump the boundary field together with the internal field. As discussed above (and in Appendix A.1), a combination of the boundary field with the internal field will result in an increased level of slowly varying contributions in the corrected field. The practical impact of this definition on the final field-to-source QSM inversion likely depends on the inversion approach employed. If the inversion algorithm is able to place sources directly at the outside boundary of the ROI, the boundary field should have a minimal impact on the calculated susceptibility distribution within the ROI. However, this has yet to be studied systematically and a detailed discussion of the susceptibility of the different QSM inversion approaches toward residual background or boundary fields is beyond the scope of the present article.

Mathematical properties of internal and background fields

It follows from the first principles of electrodynamics that, in the absence of susceptibility heterogeneity and macroscopic currents, magnetic fields satisfy the homogeneous wave equation [1]. For a static magnetic field H this equation simplifies to Laplace's equation:

$$\nabla^2 H - c^{-2} \underbrace{\frac{\partial^2}{\partial t^2} H}_{=0\,(\text{static})} = 0, \quad (1)$$

where c is the speed of light, t denotes time, and the operator $\nabla^2 = \frac{\partial^2}{\partial x^2} + \frac{\partial^2}{\partial y^2} + \frac{\partial^2}{\partial z^2}$ is the three-dimensional Laplacian, expressed here in Cartesian coordinates. Functions that satisfy Laplace's equation are called *harmonic functions* and have been extensively studied in the field of potential theory [13]. In regions with susceptibility variations, $\nabla\chi \neq 0$, the Laplacian of the total magnetic field is given by [14]

$$\nabla^2 H = H_0 \cdot \frac{1}{3} \left(\partial^2 \chi / \partial x^2 + \partial^2 \chi / \partial y^2 - 2\partial^2 \chi / \partial z^2 \right), \quad (2)$$

where H_0 is the nominal field strength of the applied main magnetic field.

It follows from Eq. (2) that the background field is harmonic *within* the ROI because the ROI does not contain any of its sources by definition. Consequently, the background field satisfies Laplace's equation inside the ROI and Poisson's equation outside the ROI:

$$\nabla^2 H_{\text{bkg}} = \begin{cases} 0 & \forall \vec{r} \in \Omega \\ H_0 \cdot \frac{1}{3} \left(\partial^2 \chi_{\text{bkg}} / \partial x^2 + \partial^2 \chi_{\text{bkg}} / \partial y^2 - 2\partial^2 \chi_{\text{bkg}} / \partial z^2 \right) & \forall \vec{r} \notin \Omega, \end{cases} \quad (3)$$

where Ω denotes the ROI. The internal field, H_{int}, has no sources outside the ROI *by definition*, and, hence, per Eq. (1), it satisfies Laplace's equation *outside* of the ROI and the Poisson equation *inside* the ROI:

$$\nabla^2 H_{\text{int}} = \begin{cases} H_0 \cdot \frac{1}{3} \left(\partial^2 \chi_{\text{int}} / \partial x^2 + \partial^2 \chi_{\text{int}} / \partial y^2 - 2\partial^2 \chi_{\text{int}} / \partial z^2 \right) & \forall \vec{r} \in \Omega \\ 0 & \forall \vec{r} \notin \Omega, \end{cases} \quad (4)$$

The mathematical properties of Eqs. (1) to (4) represent the ultimate theoretical basis of current background field correction algorithms. The following sections discuss the implications of these properties for the theoretical separability of internal and background fields as well as numerical solution strategies.

Separability of internal and background fields

To the best of our knowledge, it has yet to be determined theoretically whether a separation of the total field based on Eqs. (1) to (4) yields unique background and internal fields or if the separation is ambiguous and additional assumptions are required to obtain a physically meaningful separation. In particular, it is important to understand if internal fields can be

incorrectly attributed to the background fields, because this attribution could remove potentially important information about the susceptibility distribution within the ROI. It is also important to understand if background fields may be incorrectly attributed to the internal field. While it is likely that this incorrect attribution would have a negligible effect on QSM (because the inversion algorithms could potentially explain such contributions as magnetic susceptibility variations outside the ROI) it would have important consequences for a comparative evaluation of background removal algorithms.

It is clear that it is impossible (without additional assumptions) to uniquely assign internal field contributions as internal fields if identical fields can theoretically also be caused by sources outside the ROI. A unique separation of the total field into internal and background fields exists only if internal fields generally cannot be described by a combination of background fields. In more rigorous mathematical terms; a unique separation of internal and background fields requires that no internal field other than the trivial field (which is constant zero throughout space) is an element of the subspace spanned by all possible background fields.

Since the background field is generally harmonic *in the ROI* (cf. Eq. 3), it is clear that internal fields can be separated uniquely from background fields only if the internal field is not harmonic *in the ROI*; internal fields that are harmonic in the ROI cannot be distinguished from background fields. Equation (4) implies that internal fields are harmonic *within* the ROI if and only if their underlying susceptibility distribution satisfies a 2D wave equation with the z-coordinate as the "time" coordinate in the ROI:

$$\partial^2 \chi_{\text{int}}/\partial x^2+\partial^2 \chi_{\text{int}}/\partial y^2-2\partial^2 \chi_{\text{int}}/\partial z^2=0. \quad (5)$$

Internal fields that satisfy Eq. (5) would be harmonic not only outside the ROI but in the whole space. The question is: Do fields exist that are harmonic in the whole space? We show in Appendix A.2 that such fields are constant zero. Consequently, non-zero *harmonic* internal fields do not exist. In other words, internal fields can generally be understood as the *non-harmonic* component of the total (susceptibility-based) field perturbation.

The fact that non-zero harmonic internal fields do not exist implies that a *unique* separation of internal and background fields is possible. As a consequence, background elimination methods that employ the relations in Eqs. (1) to (4) to remove all harmonic components do not remove *any* information about the internal field.

Liu et al. [15] have illustrated in a numerical simulation that (inside the ROI) internal fields are generally only approximately orthogonal to background fields and non-orthogonality increases with decreasing distance from the boundary of the ROI. This lack of perfect orthogonality implies that background correction methods which employ projection techniques (i.e. which rely on orthogonality; see Appendix A.3) can project some field *components* of sources located inside the ROI and close to the boundary (internal fields) onto the space of background fields. In other words, the corrected field contains spurious background contributions and is not *strictly* an internal field. However, while this limitation

may *attenuate* internal fields emerging from sources close to the boundary, it does not imply that the fields cannot be uniquely separated. Our previous foundations on the harmonic properties show that a complete *elimination* of the field of internal sources will not occur.

While the contamination of the corrected field with fields that are harmonic in the ROI is of theoretical interest, it is yet unclear how it affects the field-to-source inversion of QSM. Most sophisticated (spatial domain) susceptibility mapping algorithms can place susceptibility variations outside the ROI, allowing the attribution of harmonic fields in the ROI to sources outside the ROI.

Mathematical solution of the background correction problem

Application of the Laplacian to the total field, $H = H_{\text{bkg}} + H_{\text{int}}$, results in a Poisson equation:

$$\nabla^2 H = \nabla^2 (H_{\text{bkg}} + H_{\text{int}}) = \nabla^2 H_{\text{int}}, \text{within } \Omega. \quad (6)$$

Due to its harmonic property in Ω (cf. Eq. 3), the background field does not appear on the right hand side of Eq. (6), illustrating that the Laplacian eliminates all harmonic fields in Ω. In other words, the null-space of the Laplacian in Ω is spanned by all possible harmonic fields in Ω. Solution of the Poisson equation may theoretically reveal the internal field, H_{int}. However, Eq. (6) is an under-determined problem without a unique solution. The internal field can only be determined up to the null-space of the Laplacian, i.e. up to an unknown additive harmonic field, because adding any harmonic field to H_{int} will still satisfy Eq. (6). For example, a trivial solution of Eq. (6) is the total field itself: $H_{\text{int}} = H$. However, the under-determination of Eq. (6) is not to be confused with the uniqueness property of the background-elimination problem (see above). Equation (6) is under-determined because it describes the relation between the total field and the internal field *only within* Ω, but does not include the constraint that the internal field is harmonic *outside* Ω (by definition; cf. Eq. 4).

Solving differential equations generally requires defining conditions on the boundary of their definition space. The definition of the boundary field suggests employing a derivative boundary condition:

$$\nabla^2 H_{\text{int}}(\vec{r}) = 0 \quad \forall \vec{r} \in \partial\Omega, \quad (7)$$

where ∂Ω denotes the boundary of Ω (cf. Fig. 1). The boundary condition in Eq. (7) may be implemented and the validity of Eq. (6) extended from Ω to all space by introducing a mask operation to the left-hand side of Eq. (6) [16]:

$$M \cdot \nabla^2 H = \nabla^2 H_{\text{int}}, \quad (8)$$

where M denotes a corresponding mask that sets to zero values outside the ROI and on the boundary. Solution of the Poisson equation in Eq. (8) by applying the inverse Laplacian in

the whole space theoretically gives a unique solution H_{int} with $\lim_{\|\vec{r}\|_2\to\infty} H_{\text{int}}(\vec{r})=0$, in accordance with the physical behavior of the internal field. Being harmonic outside the ROI and on the boundary, the solution of Eq. (8) satisfies the conditions of the internal field in Eqs. (1–4) and is, hence, the *unique* solution of the background correction problem.

Corollaries of Green's theorem

Green's theorem is one of the fundamental theorems of vector calculus [13], and one which has several interesting corollaries of relevance for harmonic functions. The *uniqueness* theorem and the *spherical mean value (SMV)* or *average value* theorem are the basic properties of mathematical physics used by several of the background field correction algorithms reviewed in the following sub-sections.

The *uniqueness theorem* states that a harmonic function $u(\vec{r})$ in a region Ω (such as the background field in the ROI) is uniquely defined by its values on the boundary of the region [13], $u|_{\partial\Omega}$, where $\cdot|_{\partial\Omega}$ is shorthand notation for values on the boundary.

The *SMV theorem* states that the mean value of a harmonic function calculated over a sphere centered at $\vec{r}_0$ (the SMV) equals the value of the harmonic function at the center of the sphere $u(\vec{r}_0)$:

$$\int u(\vec{r}) \cdot S(\vec{r}-\vec{r}_0)d^3\vec{r}=u(\vec{r}_0), \quad (9)$$

where $S(\vec{r})$ describes a spatially restricted, normalized ($\int S(\vec{r})d^3\vec{r}=1$) spherical function around the origin.

PRACTICAL CONSIDERATIONS REGARDING THE DEFINITION OF THE ROI

The ROI defines which sources are considered as background sources and, hence, has a critical effect on the calculated internal field. If the ROI is defined too small, important tissue regions may not be encompassed and would not be open to interpretation in subsequent susceptibility mapping steps. If the defined ROI exceeds the actually desired ROI, e.g. the brain, and includes regions that contain sources usually regarded as background sources (such as the sinus cavities), the corrected field will not meet the expectation of absence of large-scale field variations. In particular, the inclusion of voxels with erroneous field values, such as regions with severe phase noise due to low magnitude MRI signal, can have a detrimental effect on the calculated internal field [17] when those voxels are located close to or in the boundary region.

Although the definition of the ROI is critical for the outcome of QSM, the authors are not aware of any work that specifically addresses ROI generation *in vivo*. In brain imaging, the ROI is usually defined using automatic brain extraction tools for magnitude images [18], followed by a rather conservative erosion of the resulting binary brain mask. However, our experience is that automated brain extraction tools tend to perform poorly in the case of very abnormal brain anatomy, e.g. in the case of a signal-void brain lesion close the brain's surface. This represents a critical obstacle for the clinical translation of QSM. Furthermore,

at ultra-high magnetic field strength, current algorithms often fail even in healthy subjects because of strong inhomogeneities in the magnitude images. While enhanced segmentation algorithms or the use of phase error information within QSM may mitigate these effects [19], robust techniques are critically needed to automatically determine the reliability of field measurements and accurately define the ROI.

DIRECT SOLUTION OF EQUATION (8)

Since the discrete Laplacian can be calculated via convolution (symbol *) with a *kernel* κ, $\nabla^2 \rightarrow \kappa * H$, the masking in Eq. (8) allows a numerical solution via direct inverse filtering deconvolution (symbol $*^{-1}$),

$$H_{\mathrm{corr}} = \kappa *^{-1} \left(M' \cdot (\kappa * H) \right) \quad (10)$$

enabling a highly efficient numerical implementation via the Fourier convolution theorem [20]:

$$H_{\mathrm{corr}} = \mathrm{FT}^{-1} \left\{ \mathrm{FT}(M' \bullet \nabla^2 H) / \mathrm{FT}(\kappa) \right\} \quad \text{with} \quad \nabla^2 H = \mathrm{FT}^{-1} \left\{ \mathrm{FT}(H) \bullet \mathrm{FT}(\kappa) \right\}, \quad (11)$$

where FT and FT^{-1} denote the Fourier transform and the inverse Fourier transform, respectively, and ● denotes point-wise multiplication. The mask M' is designed such that it sets to zero all voxels for which the numerical calculation of the Laplacian requires voxels outside the ROI. The quantity H_{corr} is the calculated (corrected) internal field; we will use the subscript “corr” in the remainder of this article to emphasize that underlying assumptions and approximations of background correction algorithms may result in fields that do not strictly satisfy our definition of the internal field. Implications of the numerical solution outlined in Eqs. (10) and (11) for the resulting corrected field will be discussed below.

According to Eq. (11), numerical implementation of this direct approach involves the following simple steps: i) 3D Fourier transformation of the field, ii) point-wise multiplication of the Fourier-transformed field map with the Fourier-space Laplacian kernel according to Eq. (11), iii) inverse Fourier transformation, iv) masking with the eroded ROI mask that sets all voxels in the boundary region to zero, v) Fourier transformation of the masked image, vi) point-wise division by the Fourier-space Laplacian kernel (deconvolution) and setting all coefficients for which the division is not defined (kernel equals zero) to zero, and, finally, vii) inverse Fourier transformation. All Fourier transform calculations are usually performed with numerically efficient Fast Fourier Transform (FFT) algorithms. Steps (i) to (iii) may also be carried out in the spatial domain using the wrap insensitive Laplacian calculus (see [16] or Robinson et al. [21] in this same issue), which obviates the need for prior phase unwrapping. Appropriate zero-padding in the spatial domain may be introduced before step v) to reduce circular convolution artifacts, which may result in low frequency field inhomogeneities.

The binary masking involved in Eqs. (10) and (11) has implications for the voxels immediately at the inner boundary of the eroded ROI, because the Laplacian at these locations is *calculated* using the values of H within the boundary region. Sources within the boundary region, such as pial veins in the brain, affect the Laplacian's values at locations in the eroded ROI (see Figure 1). While the masking strictly enforces the boundary condition in Eq. (7), the numerically calculated Laplacian values at the inside border between boundary region and eroded ROI are inconsistent with the boundary condition. This is a source of artifacts when evaluating Eqs. (10) and (11). The inconsistencies can be particularly severe when field measurement errors exist in the boundary region, such as phase unwrapping errors. Associated artifacts in the corrected field appear as remnant background fields, because they emerge from the boundary region and are, therefore, harmonic at a distance of more than one voxel from the boundary.

As can be seen in Eq. (10), the direct solution appears as an inverse filtering approach of a spatially masked Laplacian of the total field. The multiplication with the Fourier transformed Laplacian kernel on the right-hand side of Eq. (11) is a formal point-wise multiplication by k^2, where k denotes the distance to the origin in the spatial frequency domain. Likewise, the deconvolution performed using the inverse Laplacian is a multiplication with $1/k^2$ and is, as such, not well-defined, resulting in error amplification for small spatial frequencies in the corrected field. This suggest the definition of some sort of regularized inverse Laplacian that mitigates artifacts. Schweser et al. [16] mitigated background field contamination and artifacts by using truncated singular value decomposition (TSVD) regularization, which essentially means that Fourier coefficients of the calculated internal field are set to zero wherever the corresponding magnitude of the Fourier coefficient of the deconvolution kernel falls below a certain user-defined numerical threshold. The practical effect of TSVD is similar to a mild high-pass filter which not only suppresses artifacts but also eliminates other slowly varying contributions, such as non-harmonic [22, 23] B_1-related phase offsets [24] (see Robinson et al. [21] in this same issue). In the literature, the TSVD threshold value has been chosen empirically based on the visual appearance of the internal field. A more systematical investigation is presented by Özbay et al. [25] in this special issue. Other types of regularized inverse Laplacian have been proposed with different properties [26].

The direct solution by inverse Laplacian filtering (Eq. 11) has been applied by several groups due to the simplicity of realizing an implementation [27, 28]. If the quality of the input field map is high, this method seems to eliminate background fields reasonably well, resulting in susceptibility maps with a high visual quality [16].

ASSUMPTION OF NO SOURCES CLOSE TO THE BOUNDARY (NOS)

Sophisticated Harmonic Artifact Reduction for Phase (SHARP)

The high sensitivity of the direct solution toward sources in the boundary region may be mitigated by assuming that an extended region close to the boundary of the ROI is free of any sources. This assumption allows a numerically efficient calculation of the internal field via the SMV theorem, a technique termed Sophisticated Harmonic Artifact Reduction for Phase (SHARP) [29].

The convolution-type nature of Eq. (9) allows the SMV to be expressed for all spatial locations as a convolution relation: $u * S = u$. It follows from the harmonic property of background fields that they are invariant under convolution with a spherical kernel, $H_{bkg} * S = H_{bkg}$, which allows the background field to be eliminated by subtracting its SMV from the total field [29]:

$$H - H * S = H_{bkg} + H_{int} - (H_{bkg} * S + H_{int} * S) = H_{int} - H_{int} * S. \quad (12)$$

Rewriting Eq. (12) with a modified spherical kernel $S' = \delta - S$, where δ is a Dirac distribution (unit impulse) at the center of the sphere, allows the background elimination problem to be expressed using a boundary condition similar to that in the direct solution by inverse Laplacian filtering in Eq. (6):

$$M'' \cdot (S' * H)(\vec{r}) = (S' * H_{int})(\vec{r}), \quad \text{assuming} \quad S' * H_{int} = 0 \ \forall \vec{r} \in \tilde{\Omega}'. \quad (13)$$

Analogous to the Laplacian, S' is a physically motivated filter that completely eliminates harmonic fields wherever it can be evaluated in Ω. Note that the boundary region $\tilde{\Omega}'$ and the mask M'' are different from those in the previous sub-section. Since the SMV cannot be evaluated close to the boundary, where the sphere would exceed the ROI, the widths of the boundary region, $\tilde{\Omega}'$, depends on the spatial extent of S'. In particular, since the convolution kernel S' is larger than the Laplacian kernel, the internal field can be determined only in a smaller region.

Equation (13) can be solved analogously to Eq. (6) and the numerical implementation is also analogous to the direct solution, with the spherical kernel instead of the Laplacian kernel. When SHARP is applied to data with an anisotropic voxel size, the voxel size of the utilized grid has to be taken into account when rendering the numerical spherical kernel S'. This requirement generally turns the spherical (physical) kernel into an ellipsoid numerical kernel. Alternatively, an isotropic grid can be used by resampling the total field map to isotropic voxel size before applying the algorithm.

SHARP is subject to the same problems and limitations associated with the masking step as the direct solution. In particular, violations of the boundary condition in Eq. (13) (which is extended compared to the boundary region in Eq. 7) can lead to artifacts in the corrected field. The condition can be violated by an underlying susceptibility distribution that does not satisfy $S' * H_{int} = 0$ in $\tilde{\Omega}'$, e.g. anatomical structures with different susceptibilities in this region. While the violation due to the larger kernel and the larger boundary region seem like a disadvantage of SHARP compared to the direct solution, the averaging property of the larger kernel actually mitigates artifacts resulting from the inconsistencies in the vicinity of the boundary, generally resulting in a less inhomogeneous internal field [30], and, hence, requiring less TSVD regularization. An explanation for this observation is that the averaging property of the SMV makes it more difficult to violate the boundary condition or produce net inconsistencies at the boundary compared to a much smaller Laplacian kernel (Eq. (7)).

SHARP was one of the first analytical background correction techniques to be developed and has been widely implemented and applied. While robustly eliminating the background field, a major downside of the method is the inability to determine even approximate internal field values in a relatively extended boundary region. However, since the physical extent of the boundary region is related to the grid voxel size (rendering of the numerical sphere), it can be minimized by spatial interpolation of the discretized field data before the background removal. The most native spatial interpolation in MRI is zero-padding in *k*-space, ideally applied to the measured single-channel data before multi-channel combination.

Extended SHARP (E-SHARP)

Extended SHARP (E-SHARP) [31] aims to extrapolate the SHARP-corrected field to the boundary region. The method exploits the analyticity of harmonic functions [31], which means that they can be described by a convergent power series. E-SHARP calculates a low-order Taylor expansion of the SHARP-background field based on the values of the background field in the vicinity of the boundary of the eroded ROI. However, although harmonic functions are analytical, not every analytical function is harmonic, meaning that the extrapolated background field may not coincide with the real background field.

The introduction of background correction algorithms that provide internal field values much closer to the ROI boundary (see below) have diminished the interest in a dedicated extrapolation post-processing step, explaining why E-SHARP has not been applied widely.

Variable-radius SHARP (V-SHARP)

The selection of the spatial extent of the kernel S' (sphere radius) in the original SHARP method represents a trade-off between boundary-related artifacts in the internal field (small radii) and a loss of field information at the boundary of the ROI due to its erosion (large radii). To achieve a better compromise between the two, Wu et al. [30] used a variable radius sphere for the convolution in Eq. (13). A large sphere was used for voxels sufficiently far away from the boundary of the ROI. For voxels close to the boundary, the largest possible sphere was used that allowed the convolution to be evaluated without extending over the boundary. The deconvolution was carried out with the deconvolution kernel corresponding to the largest sphere used in the convolution step. This procedure resulted in maximum accuracy in the inner part of the ROI (the region where corrected field values are obtained with the conventional SHARP method) and mitigated deconvolution artifacts resulting from violation of the boundary condition and data inconsistency at the boundary (as discussed above for SHARP).

The combination of small and large spheres has the desirable effect that corrected field values can be obtained closer to the ROI boundary and, at the same time, artifacts due to the masking-related inconsistencies are reduced. However, the use of different spheres results in a higher numerical complexity because it precludes direct Fourier-based computation. In addition, the accuracy of V-SHARP's corrected field can be expected to gradually decrease when the distance from the boundary decreases, due to the mismatch between convolution and deconvolution kernels.

V-SHARP has been widely implemented and has replaced the conventional SHARP method in most labs. An implementation of V-SHARP for MATLAB (The MathWorks, Natick, MA) is available as part of the STI Suite software package [32].

ASSUMPTION OF NO HARMONIC (NOHA) INTERNAL AND BOUNDARY FIELDS IN THE BOUNDARY REGION

The uniqueness theorem of potential theory (see above) allows calculating the background field *throughout* the ROI based on an estimate of the background field *at the boundary* of the ROI. However, the background field at the boundary is usually unknown *a priori*. Assuming both *constant zero* internal and boundary fields throughout the boundary region, the total field, H, may be used as an estimate of the background field in this region [33, 17].

Wen et al. [33] determined the background field by solving the equation $S' * H_{\text{bkg}} = 0$ in the ROI using the Jacobi iterative method [17, 9], $H_{\text{bkg}}^{(n+1)} = S * H_{\text{bkg}}^{(n)}$, and using the total field, H, for initialization of the algorithm. In this method, dubbed the *Iterative Spherical Mean Value* (iSMV) method, the boundary constraint is enforced by replacing in each iteration step the background field values in the boundary region with the total field. Provided the background field estimate is accurate in the boundary region, this algorithm converges to the true background field, gradually blurring out the internal field present in the initial starting pattern. A disadvantage of iSMV is the relatively low convergence rate of the Jacobi method.

Zhou et al. [17] solved the boundary value problem using a full multigrid (FMG) solver for elliptic partial differential equations, resulting in substantially improved computational performance while essentially yielding the same results as iSMV (when a Laplacian kernel is used instead of S'). This method is referred to as the *Laplacian Boundary Value* (LBV) method. A MATLAB implementation of LBV is available as part of the Cornell QSM software package [34].

The assumption of constant zero internal and boundary fields is required, because the background field cannot be measured without contamination from internal and boundary sources. However, relying on the uniqueness theorem, the NOHA methods implicitly assume that the background field is harmonic throughout the boundary region. Consequently, it may be expected that the solution depends *primarily* on the harmonic part of the field in the boundary region. Non-harmonic contributions from sources located in the boundary region should have a reduced effect on the solution compared to other methods [17], whereas harmonic contributions in the boundary region that emerge from sources located inside the ROI or the boundary region (such as internal fields from veins located close to boundary) affect the solution. Hence, the employed assumption of constant-zero fields is actually an assumption of *no harmonic* (NOHA) internal and boundary fields in the boundary region. A contamination of the background field estimate at the boundary with (harmonic) internal or boundary fields is likely to propagate to the corrected field. However, it is difficult to theoretically predict the actual impact of this contamination on the corrected field. It may be speculated that a violation of the NOHA assumption has a rather long-ranging effect, due to the non-local relation between sources and field perturbation.

The assumption underlying the NOHA methods is similar (but not identical) to the assumption underlying the NOS methods. In line with the definition of the boundary region, the NOS methods yield corrected fields that do not contain contributions from sources in the boundary region, whereas the NOHA methods attribute the non-harmonic part of fields from sources in the boundary region to the corrected field and likely attenuate harmonic contributions from internal and boundary fields.

NOHA techniques have not yet been used widely, probably because the advantage over techniques proposed earlier remained unclear.

MINIMIZATION OF AN OBJECTIVE FUNCTION INVOLVING A NORM (MOIN)

Instead of employing explicit boundary conditions such as in the NOS and NOHA methods (that are easily violated in the *in vivo* setting), issues associated with the numerical solution of Eq. (8) may also be addressed by implicit assumptions, such as a small Euclidean (L_2) norm of the corrected field. The nature of these methods may be understood with the help of the Hilbert projection theorem, which is reviewed in Appendix A.3.

Projection onto the space spanned by simulated background fields

Projection onto dipole fields (PDF; part of the Cornell QSM software package) [15, 35] projects the total field onto a subspace spanned by background fields. PDF employs a source simulation strategy to model the background field subspace. More specifically, the method models background fields via a magnetic susceptibility distribution χ_{bkg} outside the ROI. In line with the definition of the background field, this simulation is achieved by employing a special type of susceptibility mapping algorithm that includes the constraint of constant susceptibility *within* the ROI [35]:

$$H_{\mathrm{corr}}=\underset{H_{\mathrm{bkg}}}{\arg\min}\|\tilde{M}\cdot H-\tilde{M}\cdot H_{\mathrm{bkg}}\|_2^2 \ \text{subject to} \ H_{\mathrm{bkg}}=d*\chi_{\mathrm{bkg}} \ \text{with} \ \chi_{\mathrm{bkg}}(\vec{r})=\mathrm{const}\,\forall\vec{r}\in\Omega, \quad (14)$$

were d is the unit dipole response function [36, 37] and $\|\cdot\|_2$ denotes the L_2 norm. The mask $\tilde{M}$ restricts the objective function to the region in which the total field, H, is known (may also be the ROI). The resulting susceptibility distribution, χ_{bkg}, does not necessarily represent a physically meaningful solution, in terms of actually representing the susceptibility distribution that caused the background field, but the difference ($H - H_{\mathrm{bkg}}$) is an estimate of the internal field.

According to the Hilbert projection theorem (see Appendix A.3) Eq. (14) may be understood as a projection of the total field onto the space spanned by all external sources that can be simulated with the employed source simulation strategy. The solution is unique and orthogonal to all background fields described by the source simulation technique. A major theoretical limitation of PDF is that it uses only a *sub*space of harmonic functions to model

the background field–those generated by dipoles outside the ROI. In other words, PDF is limited to fields that can be simulated by the employed source simulation algorithm. To the best of our knowledge, it has not yet been investigated under what conditions the employed source simulation strategy is able to properly model all harmonic fields inside the ROI. For example, it may be assumed that the external region in which dipoles are placed in PDF has to be chosen appropriately large in practice.

Several precursor techniques of PDF have been presented. Geometry-dependent artifact correction (GDAC) [38] involved supervised segmentation of the sinuses, the mastoid cavity, and the skull in additional high-resolution T_1-weighted images followed by an optimization procedure in which susceptibility values are assigned to the segments and a forward-field simulation was performed. The susceptibility values were then chosen such that they best suppressed the background field. However, GDAC required subsequent high-pass filtering because background fields were usually not eliminated completely [38]. Wharton et al. [39] modeled background fields using single dipole point-sources positioned outside the brain instead of segments as in GDAC. Using an iterative technique, the strength and location of the dipole sources was optimized. However, since this technique was also not able to completely eliminate the background contributions, the authors proposed combining it with polynomial fitting. The limited success of these early projection techniques may be understood by the much less powerful source simulation approaches compared to PDF, allowing the simulation of a much smaller subspace of background fields than PDF.

Minimum-norm corrected field

The harmonic relation in Eq. (6) may be restricted to the part of the ROI in which the Laplacian can be numerically evaluated by applying an appropriate mask to *both* sides of the equation,

$$M' \cdot \nabla^2 H(\vec{r}) = M' \cdot \nabla^2 H_{\text{int}}(\vec{r}). \quad (15)$$

Equation (15) may be understood as a relaxation of the background elimination problem in Eq. (8), overcoming the inconsistencies associated with the masking of the Laplacian at the boundary on the left-hand side of Eq. (8). Compared to the direct solution and the NOS methods, a solution in the spatial domain allows the elimination of the boundary region from the data fidelity term (right-hand side in Eq. 15), in which the convolution cannot be evaluated. However, the introduction of another mask at the right-hand side turns the equation from a problem with a unique solution into an underdetermined problem with multiple solutions. It is clear that Eq. (15) allows arbitrary values of $\nabla^2 H_{\text{int}}(\vec{r})$ outside the ROI; analog to Eq. (6), it can be seen that $H_{\text{int}} = H$ is one of the solutions.

The solution with the minimum L_2 norm,

$$H_{\text{corr}} = \arg\min_h \|h\|_2^2 \quad \text{subject to} \quad M' \cdot \nabla^2 H = M' \cdot \nabla^2 h. \quad (16)$$

may be obtained, for example, by iterative solution with the conjugate gradient (cg) algorithm [40]. This strategy requires rewriting Eq. (15) as a least-squares problem of the *normal equations* [41]

$$\nabla^2 \cdot M' \cdot \nabla^2 H = \nabla^2 \cdot M' \cdot \nabla^2 h, \quad (16b)$$

and choosing the initialization point of the iteration from the range-space of $\nabla^2 \cdot M'$ [41, 42, 43], e.g. zero. Each cycle of the cg-method creates an improved approximate solution of Eq. (16) using the operation $\nabla^2 \cdot M' \cdot \nabla^2$ within the update procedure. It can be seen from the involvement of the mask M' in this operation that all approximate (interim) solutions and the final H_{corr} are constant-zero in the external region (if zero is used as the initialization point), because the update process can create a non-zero field only in the ROI and in the boundary region, but not in the external region. Consequently, the Laplacian of the corrected field can be non-zero both in the boundary region and in voxels of the external region that are adjacent to the boundary region. The non-zero Laplacian in these regions is the major difference compared to the direct solution (Eqs. 10 and 11), which allows the algorithm to compensate for spurious field inhomogeneities resulting from the inconsistencies of the numerically calculated Laplacian at the boundary of the mask M' (as discussed above for the direct solution). However, the non-zero Laplacian in these regions also implies that the corrected field is not necessarily harmonic everywhere in the boundary and external regions. In other words, the ability to place sources in the boundary region and the external region enables overfitting of internal fields with boundary and background sources, similar as to PDF (approximate orthogonality).

A possible improvement of the algorithm to mitigate boundary effects is the attenuation of the Laplacian of the field at the boundary of the mask M'. This attenuation may be seen as a spatial filtering reducing the truncation effects of the binary masking at the boundary and would lead to approaches with different masks on the right and left hand sides of Eq. (15). A larger mask (e.g. one that does not set to zero voxels in the boundary region) for the corrected field on the right-hand side of Eq. (15) enforces harmonic properties in the boundary region.

Yielding a corrected field that is constant-zero in the *external* region, the minimum-norm solution appears similar to the NOHA solutions, which employ the practically motivated assumption of constant-zero internal and boundary fields throughout the *boundary* region. In other words, the minimum-norm solution shifts the region for the constant-zero constraint farther away from the ROI. However, as discussed above, while NOHA methods use the constant-zero assumption as a starting point for the solution, they effectively rely on the *harmonic* part of the field in the boundary region to estimate the background field, rendering a direct comparison between the methods difficult.

A major difference between PDF and Eq. (16) is that Eq. (16) minimizes the norm of the corrected field throughout *all space*, including the space outside the ROI, whereas PDF minimizes the norm of the calculated field only within the region defined by the mask $\tilde{M}$.

The incorporation of the corrected field outside of the ROI has a penalizing effect on the attribution of fields originating from sources inside the boundary region as internal fields (rather than as external fields; see discussion of PDF).

The minimum-norm method was first proposed by de Rochefort et al.[2] [44] who also replaced the mask M' in Eq. (16) with a weighting function that masked the external region and additionally accounted for varying noise in the total field H within the ROI (more precisely using the error on the Laplacian calculated with error propagation rules). The incorporation of a weighting function, which is enabled by the iterative implementation (as compared to the direct solution), allows penalizing regions in which the Laplacian is particularly noisy and accelerates convergence in regions with low noise levels. A MATLAB implementation of this algorithm is available online [45].

Minimum-norm of the (filtered) Laplacian throughout all space

A problem very similar to Eq. (16) is the calculation of the field with a minimum-norm *Laplacian*:

$$L_{\min} = \arg\min_{L} \|L\|_2^2 \ \text{subject to} \quad M' \cdot \nabla^2 H = M' \cdot L. \tag{17}$$

The solution is the Laplacian of the background-corrected field throughout all space. The corrected field is obtained from the solution of Eq. (17) by applying the inverse Laplacian. The only mathematical difference between this problem and the problem in Eq. (16) is that the norm of the Laplacian of the field is minimized compared to the norm of the field itself.

We see that any variation of the Laplacian of the corrected field outside the ROI would increase the objective function in Eq. (17). Hence, similar to the minimum-norm problem in Eq. (16), the solution, $L_{\min}$, of Eq. (17) will always be zero everywhere outside of the ROI guarantying that the solution will have the desired harmonic properties outside the ROI and in the boundary region, regardless of the initialization of the solution algorithm (which may also be understood with the help of the projection theorem, see Appendix A.4). Hence, Eq. (17) is equivalent to the Laplacian direct deconvolution in Eqs. 10 and 11.

HARmonic (background) PhasE REmovaL using the Laplacian operator (HARPERELLA; part of the STI Suite software package) [46] solves a variant of Eq. (17) that focusses the minimization to certain frequency-domain features of the Laplacian of the field via the introduction of filtering with a kernel F:

[2] In their original work the authors formulated the problem as a least-squares problem without acknowledging the importance of the initialization value to mitigate the under-determination problem outside the ROI.

$$L_{\min}=\arg\min_{L}\|F*\left(\underbrace{M'\cdot\nabla^2H+(1-M')\cdot L}_{=L'}\right)\|_2^2$$
$$=\arg\min_{L}\|F*(M'\cdot\nabla^2H)-F*[(M'-1)\cdot L]\|_2^2 \quad (18)$$

(see Appendix A.3 for an illustration of the similarity between Eqs. 17 and 18).

The filter kernel F has a direct effect on the solution obtained. A sharpening kernel generally penalizes rapid variations in L', whereas a smoothing kernel penalizes only large-scale changes of L' but tolerates rapid (noise-like) variations, and the Dirac reduces the problem to Eq. (18). Since the Laplacian may itself be understood as a filter (convolution with the Laplacian kernel κ, see Eq. 10) and linear filters are commutative, the filter F may be understood as acting directly on the calculated internal field, penalizing rapid or large-scale variations of the calculated field. In their original publication [46], the authors used the SMV kernel S as a filter, which effectively acts as a spatially restricted smoothing kernel, penalizing large-scale inhomogeneities in the corrected field.

Comparison of Eqs. (18) and (A.2) illustrates that the problem projects the filtered, masked Laplacian of the total field onto the space spanned by all filtered functions with non-zero function values *before* filtering *only* outside of the ROI. This subspace is not generally an orthogonal complement of the subspace spanned by all internal fields. The orthogonality decreases the more spatially extended is the filter kernel F and the solution of Eq. (18) will be non-zero outside the ROI if a filter kernel is used that relaxes the orthogonality requirement. Such a filter kernel will create fields that are harmonic inside the ROI to suppress field inhomogeneities resulting from the boundary, which can result in a deviation of the corrected field from the true internal field within the ROI.

With iHARPERELLA, Li et al. [47] proposed using the inverse Laplacian kernel, κ^{-1}, as a filter in HARPERELLA, which projects the direct solution (Eq. 10 and left-hand side in norm of Eq. 18) onto the subspace spanned by all external fields. This additional projection can be expected to reduce residual field inhomogeneities relating to the issues inherent with the masking and the numerical deconvolution in Eqs. 10 and 11. iHARPERELLA has been observed to more effectively suppress spatially slowly varying contributions than HARPERELLA with a spherical kernel [47]. This observation may be explained by the fact that the inverse Laplacian kernel is not spatially localized, creating an effect throughout all space, compared to only the local neighborhood when using the SMV kernel in HARPERELLA.

Regularization-enabled SHARP (RESHARP)

A relaxed definition of background contributions would go beyond our magneto-static definition and include all unwanted MRI phase effects in the ROI that, if they would not be eliminated, would have an undesirable effect on the QSM analysis within the ROI. In particular, these effects include all contributions that are not caused by magnetic

susceptibility and, hence, do not satisfy Eq. (2), such as relatively slowly varying B_1-related phase offsets (see Robinson et al. [21] in this issue). While a correct phase-based measurement of the total field, *H*, should in principle not show such contributions, phase images in practice often suffer from spurious B_1-field contributions [21]. The background correction algorithms discussed above generally eliminate the *harmonic* components of these additional contributions. However, non-harmonic contributions are generally interpreted as internal fields with these techniques [25]. To allow for the compensation of such non-harmonic contributions in the field data, Sun and Wilman [48] formulated the background correction problem as an optimization problem with Tikhonov regularization:

$$H_{\text{corr}}=\arg\min_{h}\|M\cdot[(H-h)*S']\|_2^2+\lambda\cdot\|h\|_2^2, \quad (19)$$

where $\|\cdot\|_2$ denotes the Euclidean norm and $\lambda$is the Tikhonov regularization parameter. The term on the left hand side of the objective function in Eq. (19) promotes a harmonic background field within the ROI (excluding the boundary region). The second term on the right hand side penalizes the norm of the internal field. The modified SMV kernel S' may in principle be replaced by the Laplacian kernel.

The regularization parameter, λ, defines a trade-off between a background field that is harmonic and a small norm of the internal field. For $\lambda\to\infty$, the trivial solution is obtained, $H_{\text{corr}} = 0$. For $\lambda\to 0$ the solution converges to the least-norm solution in Eq. (16), and for $\lambda = 0$ a unique solution of Eq. (19) does not exist because an arbitrary harmonic field can be added to the internal field, while still satisfying the equation (analog to Eq. 15). Due to the weighting of the two terms in Eq. (19), the background field corresponding to the solution of Eq. (19) is generally not strictly harmonic, as long as $\lambda \neq 0$, which allows the suppression of non-harmonic contributions such as B_1-related phase offsets but, on the other hand, sacrifices the accuracy of the internal field because also the internal field is non-harmonic and will be suppressed. A reasonable trade-off can be achieved by techniques such as L-curve optimization. RESHARP has been shown to produce more reliable results close to the boundaries of the ROI than the original SHARP method when the same kernel S' is employed [48]. A MATLAB implementation of RESHARP is available on GitHub [49].

A QUANTITATIVE COMPARISON

To quantitatively compare the different background elimination approaches discussed in this review we applied, in collaboration with the authors of the respective original publications, all methods to the brain field of a realistic numerical human torso model. The numerical model allowed us to compare the corrected fields against a ground truth.

Materials and Methods

We used the same model as Özbay et al. [25] (in this special issue); details about the model generation and field simulation can be found therein. Figure 3 (top row) illustrates the model. The ground truth was obtained by simulating the field perturbation of the brain susceptibility model with no susceptibility variations outside the brain.

To obtain the best possible results for each technique, the authors of the respective original publications applied their algorithms to the total field within the brain: HARPERELLA and iHARPERELLA (W.L.), LBV, iSMV, and PDF (Dong Zhou from Yi Wang's group), direct solution, SHARP and V-SHARP (F.S.), minimum norm solution (L. de R.), RESHARP (Hongfu Sun from Alan Wilman's group). Each participating group was provided with i) a binary mask defining the ROI, ii) the ROI-masked total field, iii) the ground truth internal field, and iv) a set of 32 binary masks with which to assess the quality of the calculated internal field. The masks defined brain-shaped shells of 1 mm thickness located between 1 and 32 mm from the brain's surface (in steps of 1 mm; for details please see Özbay et al. [25]). The ground truth was provided to achieve the optimal possible result with each technique, allowing each collaborator to optimize parameters of their technique, if required. We considered the practical question of finding the optimal set of parameters in each method as beyond the scope of the experiment. To standardize the parameter optimization, we provided a script that calculated the normalized root mean square error (NRMSE) between the ground truth and the reconstructed internal fields as a function of the distance from the brain's surface. To this end, the RMSE was calculated in the 32 provided brain shells and normalized by dividing by the number of voxels in each respective shell. The parameter that resulted in the smallest sum of all 32 NRMSE values was considered optimal.

For RESHARP, we varied the regularization parameter, λ, over a range from 0 to 1, with 13 exponentially spaced steps between 10^{-6} and 1. For the direct solution we employed the improved universal regularization scheme proposed by Özbay et al. [25] (in this issue) using cut-off frequencies between 0.001 and 0.05 mm^{-1} (in steps of 0.001 mm^{-1}). For SHARP and V-SHARP we used values between 0.001 and 0.02 mm^{-1} (steps of 0.001 mm^{-1}) and tested (maximum) radii between 2 and 15 mm (in steps of 1 mm). For LBV 1mm thick (one voxel) boundary region was used. iSMV was applied with a Laplacian kernel instead of an SMV-kernel to produce results comparable to LBV.

For comparison purposes we also applied homodyne correction [50] which is often used for heuristic background field correction in Susceptibility Weighted Imaging (SWI) [51, 52, 53]. Two-dimensional homodyne-filtering was implemented with frequency domain widths of 64×64 and 32×32 voxels.

We refrained from recording the computation times of the different techniques because the algorithms were applied on different computational hardware and were implemented by different labs. Computational efficiency highly depends on the coding of the algorithm and a direct comparison of the computation times, even if the algorithms were executed on the same hardware, could result in misleading conclusions.

Results

Due to the lack of measurement errors and non-harmonic background fields in the model field, no typical L-curve shape was obtained with RESHARP. The optimal solution was obtained for $\lambda=0$, equivalent to the minimum-norm solution. For in the direct solution, SHARP, and V-SHARP obtained optimal parameters were 0.039 mm^{-1}; 0.016 mm^{-1} and 15 mm; and 0.013 mm^{-1} and 15 mm, respectively.

Figure 3 shows exemplary slices of the calculated internal fields with the different techniques, along with the respective differences to the ground truth. Figure 4 shows a plot of the NMRSE for all methods as a function of distance from the brain's surface.

Apart from their spatial support (the ROI), it was difficult to discern differences between the internal field maps obtained with the various methods in Fig. 3. All techniques yielded comparable results with relatively smooth error patterns and quantitative accuracy generally improved with the distance from the boundary of the ROI (Fig. 4). Only the direct solution showed relatively strong deviations from the ground truth, which can be explained by the (strong) regularization involved and the inconsistencies at the boundary (without regularization), respectively. All except the NOHA methods and HARPERELLA showed a localized hyper-intense inhomogeneity at the sagittal sinus (arrows) and rapidly varying errors in the direct vicinity of the boundary. This inhomogeneity may be explained by the data inconsistency at the boundary (direct solution), a breakdown of the intrinsic assumption of a source-free boundary region (V-SHARP), and the issue of only approximate orthogonality (iHARPERELLA, PDF and RESHARP), respectively. These artifacts were not visible to the same degree in SHARP because of the substantially broader boundary region. The heuristic methods showed incomplete background suppression (Homodyne 32) and considerable artifacts in the corrected field (Homodyne 64), respectively.

Discussion

Deviations are smaller in SHARP than in the direct solution with regularization because SHARP generally requires less regularization due to a more extended kernel (see above). This difference between the methods is also reflected by a large NRMSE in the quantitative analysis (Fig. 4). V-SHARP extends the definition space of the internal field map compared to SHARP and had an error pattern which looked similar to that of the other methods, but it produced less accurate values close to the boundary (arrow). While these deviations were visible on the difference image, they did not result in a substantial deviation from other methods in the quantitative analysis (straight red line in Fig. 4), where V-SHARP outperformed SHARP and was on par with the MOIN methods (blue).

The NOHA methods, iSMV and LBV, showed similar error patterns and NMRSE values, reflecting the fact that they solve exactly the same mathematical problem. Small differences between the two methods can be explained by the much slower convergence of iSMV compared to LBV; it is likely that the solutions did not converge to the exact same extent in the examples shown. These methods outperformed all other techniques in the quantitative comparison (Fig. 4, black). Instead of suffering from a highly localized inhomogeneity at the sagittal sinus, the associated error of the NOHA methods was more spread throughout the occipital part of the brain. This observation can be explained by a violation of the implicit assumption that the internal fields are zero in the boundary region.

The error pattern of HARPERELLA was similar to that of the NOHA methods and different from that of the other MOIN methods, which can be understood by recalling that iHARPERELLA, PDF and RESHARP minimize the norm of the internal field, whereas HARPERELLA (with the SMV kernel) minimizes the low-pass filtered Laplacian of the field, which necessarily results in a different solution. The spatial extent of the filter kernel

used with HARPARELLA has an effect on the approximate orthogonality that is a common issue in the MOIN methods. Using the spatially restricted SMV kernel (as in this work) qualitatively places HARPERELLA between iHARPERELLA and the NOHA methods. The NMRSE was slightly higher with HARPERELLA than with iHARPERELLA, PDF, and RESHARP, which had very similar NMRSEs. The inhomogeneity at the location of the sagittal sinus illustrates the over-fitting that is associated with MOIN solutions due to the only approximate orthogonality of internal and background fields in the ROI, resulting in the creation of background fields to minimize the norm of the internal field pattern. Upon closer inspection, the error pattern of PDF showed subtle Gibbs-like artifacts, which can be explained by a mismatch of the rendered numerical dipoles used for the creation of the model (F.S.) and for PDF (Dong Zhou), illustrating another complication of PDF: the dipole used for PDF must exactly mimic the appearance of the dipole in the field data acquired.

Conclusion

Despite the different assumptions involved in the compared background correction algorithms, differences between the obtained corrected fields were minimal. However, considering the background field elimination performance, we recommend desisting from using the direct solution and NOS methods for studying cortical regions of the brain because those methods either result in considerably degraded internal field values compared to other methods (V-SHARP and direct solution; Fig. 3) or do not produce any internal field values at all in these regions (SHARP). When using V-SHARP, results in regions with a distance less than the maximum radius of the spheres employed should generally be interpreted with caution. In deep brain regions, the performance of all methods (except the direct solution) was relatively similar and all methods may be regarded as more or less equivalent. However, we want to emphasize that the performance of all methods also critically depends on aspects of their numerical implementation. The actual numerical algorithms applied in the present multi-center study may be considered as gold-standard implementations because they were coded by the original inventors of the respective techniques. In addition, the quantitative comparison presented here aimed to identify similarities and differences between the various published techniques and to assess only how accurately the internal field can be determined. It has yet to be clarified to what degree residual background fields or (regularization) artifacts propagate into susceptibility maps. It is the authors' experience that even relatively poorly corrected field maps (e.g. due to an ROI that was too large) often result in susceptibility maps without apparent artifacts. This observation can be explained by the apparent capability of (spatial-domain based) QSM algorithms to explain certain residual background fields by susceptibility variations outside the ROI, not affecting the calculated susceptibility values inside the ROI. Özbay et al. [25] demonstrated this capability in the present special issue. A thorough investigation of the propagation of residual background fields into susceptibility maps is beyond the scope of this study and will be subject of future research.

SUMMARY

We have reviewed the current literature on background elimination algorithms for QSM (Table 1). The algorithms were classified based on the mathematical solution obtained and

assumptions involved. We have shown that the internal field can be understood as the (unique) non-harmonic component of the total field inside the ROI and, hence, that elimination of harmonic fields does not remove information about susceptibility variations inside the ROI. Furthermore, we have shown that, due to an ambiguity of the problem, susceptibility variations which occur one voxel from the boundary of the ROI (the boundary region) cannot be considered as sources of the internal field. A comprehensive comparison of the different techniques in a numerical model showed only minor differences, primarily in cortical region of the brain. Future research needs to understand the sensitivity with respect to field measurement errors as well as the relative computational complexity of the different techniques.

Acknowledgments

This research was funded by the National Center for Advancing Translational Sciences of the National Institutes of Health under award Number UL1TR001412. The content is solely the responsibility of the authors and does not necessarily represent the official views of the NIH.

We are grateful to Dong Zhou and Yi Wang from the Cornell MRI Research Lab and Hongfu Sun, Ryan Topfer, and Alan Wilman from the Peter S. Allen MR Research Centre at the University of Alberta for enabling the quantitative comparison of the background elimination approaches by being so kind as to apply their algorithms to our numerical model.

Abbreviations used

cg	Conjugate Gradient
E-SHARP	Extended SHARP
FFT	Fast Fourier Transform
FMG	full multigrid
GDAC	Geometry-dependent artifact correction
HARPERELLA	HARmonic (background) PhasE REmovaL using the Laplacian operator
iSMV	Iterative Spherical Mean Value
LBV	Laplacian Boundary Value
NOHA	No HArmonic internal and boundary fields in the boundary region
NRMSE	normalized root mean square error
PDF	Projection onto dipole fields
ppm	parts per million
QSM	quantitative susceptibility mapping
RESHARP	Regularization-enabled SHARP

RMSE	root mean square error
ROI	region of interest
SHARP	Sophisticated Harmonic Artifact Reduction for Phase
SMV	spherical mean value
TSVD	truncated singular value decomposition
V-SHARP	Variable-radius SHARP

LITERATURE

1. Schweser F, Deistung A, Reichenbach JR. Foundations of MRI phase imaging and processing for Quantitative Susceptibility Mapping (QSM). Z Med Phys. Mar; 2016 26(1):6–34. [Online]. Available: http://linkinghub.elsevier.com/retrieve/pii/-S0939388915001427. [PubMed: 26702760]
2. Li LZ. Magnetic susceptibility quantification for arbitrarily shaped objects in inhomogeneous fields. Magn Reson Med. Nov; 2001 46(5):907–16. [Online]. Available: http://www.ncbi.nlm.nih.gov/pubmed/11675642. [PubMed: 11675642]
3. Haacke, EM.Brown, RW.Thompson, MR., Venkatesan, R., editors. Magnetic Resonance Imaging - Physical Principles and Sequence Design. 1. Vol. ch. 25. New York: John Wiley & Sons, Inc; 1999. Magnetic properties of tissues: theory and measurement; p. 741-779.
4. Ericsson A, Weis J, Hemmingsson A, Wikström M, Sperber GO. Measurements of magnetic field variations in the human brain using a 3D-FT multiple gradient echo technique. Magn Reson Med. Feb; 1995 33(2):171–7. [Online]. Available: http://www.ncbi.nlm.nih.gov/pubmed/7707906. [PubMed: 7707906]
5. Wu B, Li W, Avram AV, Gho SM, Liu C. Fast and tissue-optimized mapping of magnetic susceptibility and T2* with multi-echo and multi-shot spirals. NeuroImage. Jan; 2012 59(1):297–305. [Online]. Available: http://www.ncbi.nlm.nih.gov/pubmed/-21784162. [PubMed: 21784162]
6. Liu T, Wisnieff C, Lou M, Chen W, Spincemaille P, Wang Y. Nonlinear formulation of the magnetic field to source relationship for robust quantitative susceptibility mapping. Magn Reson Med. Feb; 2013 69(2):467–76. [Online]. Available: http://-doi.wiley.com/10.1002/mrm.24272http://www.ncbi.nlm.nih.gov/pubmed/22488774. [PubMed: 22488774]
7. Liu C, Wei H, Gong N-j, Cronin M, Dibb R, Decker K. Quantitative Susceptibility Mapping: Contrast Mechanisms and Clinical Applications. Tomography. 2015; 1(1):3–17. [Online]. Available: http://digitalpub.tomography.org/i/585879-vol-1-no-1-sep-2015/3. [PubMed: 26844301]
8. Haacke EM, Liu S, Buch S, Zheng W, Wu D, Ye Y. Quantitative susceptibility mapping: current status and future directions. Magn Reson Imaging. Jan; 2015 33(1):1–25. [Online]. Available: http://www.ncbi.nlm.nih.gov/pubmed/25267705http://-linkinghub.elsevier.com/retrieve/pii/S0730725X14002926. [PubMed: 25267705]
9. Wang Y, Liu T. Quantitative susceptibility mapping (QSM): Decoding MRI data for a tissue magnetic biomarker. Magn Reson Med. 2015; 73(1):82–101. [Online]. Available: http://doi.wiley.com/10.1002/mrm.25358. [PubMed: 25044035]
10. Duyn JH. MR susceptibility imaging. J Magn Reson. Apr.2013 229:198–207. [Online]. Available: http://www.ncbi.nlm.nih.gov/pubmed/23273840. [PubMed: 23273840]
11. Li LZ, Leigh JS. Quantifying arbitrary magnetic susceptibility distributions with MR. Magn Reson Med. 2004; 51(5):1077–1082. [Online]. Available: http://-dx.doi.org/10.1002/mrm.20054. [PubMed: 15122694]
12. Schenck JF. Health and physiological effects of human exposure to whole-body four-tesla magnetic fields during MRI. Ann N Y Acad Sci. Mar.1992 649:285–301. [Online]. Available: http://www.ncbi.nlm.nih.gov/pubmed/1580500. [PubMed: 1580500]
13. Roy, KK. Potential Theory in Applied Geophysics. Vol. ch. 10. Berlin: Springer; 2008. Green's Theorem in Potential Theory; p. 307-328.

14. Bakker CJG, de Leeuw H, Seevinck PR. Selective depiction of susceptibility transitions using Laplace-filtered phase maps. Magn Reson Imaging. Jun; 2012 30(5):601–9. [Online]. Available: http://www.ncbi.nlm.nih.gov/pubmed/22406615. [PubMed: 22406615]
15. Liu T, Khalidov I, de Rochefort L, Spincemaille P, Liu J, Tsiouris AJ, Wang Y. A novel background field removal method for MRI using projection onto dipole fields (PDF). NMR Biomed. 2011; 24:1129–36. [Online]. Available: http://www.ncbi.nlm.nih.gov/-pubmed/21387445. [PubMed: 21387445]
16. Schweser F, Deistung A, Sommer K, Reichenbach JR. Toward online reconstruction of quantitative susceptibility maps: Superfast dipole inversion. Magn Reson Med. 2013; 69(6):1581–93. [Online]. Available: http://dx.doi.org/10.1002/mrm.24405http://onlinelibrary.wiley.com/doi/10.1002/mrm.24405/abstracthttp://www.ncbi.nlm.nih.gov/-pubmed/22791625.
17. Zhou D, Liu T, Spincemaille P, Wang Y. Background field removal by solving the Laplacian boundary value problem. NMR Biomed. 2014; 27(3):312–319. [Online]. Available: http://www.ncbi.nlm.nih.gov/pubmed/24395595http://doi.wiley.com/-10.1002/nbm.3064. [PubMed: 24395595]
18. Smith SM. Fast robust automated brain extraction. Hum Brain Mapp. 2002; 17(3):143–155. [Online]. Available: http://dx.doi.org/10.1002/hbm.10062. [PubMed: 12391568]
19. Wang S, Liu T, Chen W, Spincemaille P, Wisnieff C, Tsiouris aJ, Zhu W, Pan C, Zhao L, Wang Y. Noise Effects in Various Quantitative Susceptibility Mapping Methods. IEEE Trans Biomed Eng. Dec; 2013 60(12):3441–3448. [Online]. Available: http://www.ncbi.nlm.nih.gov/pubmed/23751950http://ieeexplore.ieee.org/lpdocs/-epic03/wrapper.htm?arnumber=6527319. [PubMed: 23751950]
20. Bracewell, RN. The Fourier transform and its applications. 3. McGraw-Hill Science/Engineering/Math; 2000.
21. Robinson S, Bredies K, Khabipova D, Dymerska B, Schweser F. An illustrated comparison of processing methods for phase MRI and QSM: Combining array coil signals and phase unwrapping. NMR Biomed. 2016 vol. (in review.
22. Voigt T, Katscher U, Doessel O. Quantitative conductivity and permittivity imaging of the human brain using electric properties tomography. Magn Reson Med. 2011; 66(2):456–66. [Online]. Available: http://doi.wiley.com/10.1002/mrm.22832http://www.ncbi.nlm.nih.gov/pubmed/21773985. [PubMed: 21773985]
23. Kim DH, Choi N, Gho SM, Shin J, Liu C. Simultaneous imaging of in vivo conductivity and susceptibility. Magn Reson Med. 2014; 71(3):1144–1150. [Online]. Available: http://doi.wiley.com/10.1002/mrm.24759http://www.pubmedcentral.nih.gov/articlerender.fcgi?artid=3883903&tool=pmcentrez&rendertype=abstract. [PubMed: 23606054]
24. Schweser, F., Atterbury, M., Deistung, A., Lehr, BW., Sommer, K., Reichenbach, JR. Harmonic phase subtraction methods are prone to B1 background components. Proc Intl Soc Mag Reson Med; 2011; Montreal, CA. 2011. p. 2657
25. Özbay, PS., Deistung, A., Feng, X., Nanz, D., Reichenbach, JR., Schweser, F. A comprehensive numerical analysis of background phase correction with V-SHARP. NMR Biomed. 2016. vol. (epub)[Online]. Available: http://doi.wiley.com/10.1002/nbm.3550
26. Gonzalez, RC., Woods, RE. Digital Image Processing. 1. Pearson Education, Limited; 1992.
27. Keuken MC, Forstmann BU. A probabilistic atlas of the basal ganglia using 7 T MRI. Data in Brief. 2015; 4:577–582. [Online]. Available: http://linkinghub.elsevier.com/retrieve/pii/S235234091500147X. [PubMed: 26322322]
28. Fritzsch D, Reiss-Zimmermann M, Trampel R, Turner R, Hoffmann KT, Schäfer A. Seven-Tesla Magnetic Resonance Imaging in Wilson Disease Using Quantitative Susceptibility Mapping for Measurement of Copper Accumulation. Invest Radiol. 2014; 49(5):299–306. [Online]. Available: http://www.ncbi.nlm.nih.gov/pubmed/24220252http://content.wkhealth.com/linkback/openurl?sid=WKPTLP:landingpage&an=00004424-201405000-00006. [PubMed: 24220252]
29. Schweser F, Deistung A, Lehr BW, Reichenbach JR. Quantitative imaging of intrinsic magnetic tissue properties using MRI signal phase: An approach to in vivo brain iron metabolism? NeuroImage. Oct; 2011 54(4):2789–2807. [Online]. Available: http://www.ncbi.nlm.nih.gov/pubmed/21040794http://dx.doi.org/10.1016/j.neuroimage.2010.10.070. [PubMed: 21040794]

30. Wu B, Li W, Guidon A, Liu C. Whole brain susceptibility mapping using compressed sensing. Magn Reson Med. 2011; 24:1129–36. [Online]. Available: http://www.ncbi.nlm.nih.gov/pubmed/21671269.
31. Topfer R, Schweser F, Deistung A, Reichenbach JR, Wilman AH. SHARP edges: Recovering cortical phase contrast through harmonic extension. Magn Reson Med. 2015; 73(2):851–856. [Online]. Available: http://www.ncbi.nlm.nih.gov/pubmed/24590869http://doi.wiley.com/10.1002/mrm.25148. [PubMed: 24590869]
32. Liu, C. STI Suite. 2016. [Online]. Available: http://people.duke.edu/~cl160/
33. Wen Y, Zhou D, Liu T, Spincemaille P, Wang Y. An iterative spherical mean value method for background field removal in MRI. Magn Reson Med. 2014; 72(4):1065–1071. [Online]. Available: http://www.ncbi.nlm.nih.gov/pubmed/24254415http://doi.wiley.com/10.1002/mrm.24998. [PubMed: 24254415]
34. Wang, Y. Cornell QSM software package. 2016. [Online]. Available: http://weill.cornell.edu/mri/pages/qsm.html
35. de Rochefort L, Liu T, Kressler B, Liu JS, Spincemaille P, Lebon V, Wu J, Wang Y. Quantitative susceptibility map reconstruction from MR phase data using Bayesian regularization: validation and application to brain imaging. Magn Reson Med. 2010; 63(1):194–206. [Online]. Available: http://dx.doi.org/10.1002/mrm.22187. [PubMed: 19953507]
36. Holt RW, Diaz PJ, Duerk JL, Bellon EM. MR susceptometry: an external-phantom method for measuring bulk susceptibility from field-echo phase reconstruction maps. J Magn Reson Imaging. 1994; 4(6):809–818. [Online]. Available: http://www.ncbi.nlm.nih.gov/pubmed/7865941. [PubMed: 7865941]
37. Jackson, JD. Classical Electrodynamics. 2. Vol. ch. 5.6. New York: John Wiley & Sons; 1975. Magnetic Fields of a Localized Current Distribution, Magnetic Moment; p. 180-184.
38. Neelavalli J, Cheng YCN, Jiang J, Haacke EM. Removing background phase variations in susceptibility-weighted imaging using a fast, forward-field calculation. J Magn Reson Imaging. Apr; 2009 29(4):937–948. [Online]. Available: http://dx.doi.org/10.1002/jmri.21693. [PubMed: 19306433]
39. Wharton SJ, Schäfer A, Bowtell RW. Susceptibility mapping in the human brain using threshold-based k-space division. Magn Reson Med. May; 2010 63(5):1292–304. [Online]. Available: http://doi.wiley.com/10.1002/mrm.22334http://-www.ncbi.nlm.nih.gov/pubmed/20432300. [PubMed: 20432300]
40. Hestenes M, Stiefel E. Method of conjugate gradients for solving linear systems. J Res Nat Bur Standarts. 1952; 49(6):409–436.
41. Conn, AR., Gould, NIM., Toint, PL. Trust Region Methods. Vol. ch. 5.3. SIAM; 2000. Linear Least-Squares Problems; p. 106-107.
42. Yunqing, H., Kornhuber, R., Widlund, O., Xu, J. Domain Decomposition Methods in Science and Engineering XIX. Vol. ch. 3. Springer Science & Business Media; 2010. A Least-Squares/Fictious Domain Method for the Solution of Problem (1), (2); p. 472
43. Conn, A., Gould, N., Toint, P. Trust Region Methods. Vol. ch. 5.3. SIAM; 2000. Linear Least-Squares Problems; p. 959
44. de Rochefort, L., Delzor, A., Guillermier, M., Houitte, D., Chaigneau, M., Déglon, N., Hantraye, P., Lebon, V. Quantitative Susceptibility Mapping In Vivo in the Rat Brain. Proc Intl Soc Mag Reson Med; 2010; 2010.
45. de Rochefort, L. Matlab code of minimum-norm algorithm. 2016. [Online]. Available: http://www.ir4m.u-psud.fr/spip.php?article395
46. Li W, Avram AV, Wu B, Xiao X, Liu C. Integrated Laplacian-based phase unwrapping and background phase removal for quantitative susceptibility mapping. NMR Biomed. 2014; 27(2):219–27. [Online]. Available: http://doi.wiley.com/10.1002/-nbm.3056http://www.ncbi.nlm.nih.gov/pubmed/24357120. [PubMed: 24357120]
47. Li, W., Wu, B., Liu, C. iHARPERELLA: an improved method for integrated 3D phase unwrapping and background phase removal. Proc Intl Soc Mag Reson Med; 2015; Toronto, CA. 2015. p. 3313
48. Sun H, Wilman AH. Background field removal using spherical mean value filtering and Tikhonov regularization. Magn Reson Med. 2014; 71(3):1151–1157. [Online]. Available: http://

doi.wiley.com/10.1002/mrm.24765http://www.ncbi.nlm.nih.gov/-pubmed/23666788. [PubMed: 23666788]

49. Sun, H. RESHARP on GitHub. 2016. [Online]. Available: https://github.com/-sunhongfu/QSM/blob/master/bkg_rm/resharp.m
50. Noll DC, Nishimura DG, Makovski A. Homodyne detection in magnetic resonance imaging. IEEE Trans Med Imaging. 1991; 10(2):154–163. [PubMed: 18222812]
51. Reichenbach JR, Haacke EM. High resolution BOLD venographic imaging: a window into brain function. NMR Biomed. 2001; 14(7–8):453–467. [PubMed: 11746938]
52. Reichenbach JR, Barth M, Haacke EM, Klarhöfer M, Kaiser WA, Moser E. High-resolution MR venography at 3.0 Tesla. J Comp Assist Tomogr. 2000; 24(6):949–957. [Online]. Available: http://www.ncbi.nlm.nih.gov/pubmed/11105717.
53. Haacke EM, Xu Y, Cheng YCN, Reichenbach JR. Susceptibility weighted imaging (SWI). Magn Reson Med. Sep; 2004 52(3):612–8. [Online]. Available: http://dx.doi.org/10.1002/mrm.20198http://www.ncbi.nlm.nih.gov/pubmed/15334582. [PubMed: 15334582]

APPENDIX

A.1 Susceptibility ambiguity associated with the traditional definition of internal and background fields

Let χ_{int} and χ_{bkg} be the susceptibility distributions in Ω (denoting the ROI) and in $\mathbf{R}^3$ without Ω (outside the ROI), respectively. For the sake of simplicity, we set $\chi_{\text{int}} = c_1$ for all locations not in Ω and $\chi_{\text{bkg}} = c_2$ in Ω. If we let $H_{\text{int}} = \chi_{\text{int}} * d$ (* denotes convolution and d is the unit dipole response [37, 36]) and $H_{\text{bkg}} = \chi_{\text{bkg}} * d$, then we obtain $H_{\text{int}} + H_{\text{bkg}} = \lfloor M \cdot \chi_{\text{int}} + (1 - M) \cdot \chi_{\text{bkg}} \rfloor * d + [(1 - M) \cdot c_1 + M \cdot c_2] * d$. Since we require that the sum of internal and background field equals the total field, $H_{\text{int}} + H_{\text{int}} + H_{\text{bkg}} = H$, the values of c_1 and c_2 need to be chosen such that $[(1 - M) \cdot c_1 + M \cdot c_2] * d = 0$. This condition implies that $c_1 = c_2$, which may be understood by recapitulating that a constant susceptibility throughout all space does not induce field *inhomogeneities*, i.e. $c * d = 0$ for $c = \text{const.}$ in $\mathbf{R}^3$. In other words, changing the values of χ_{int} for all locations *not in* Ω and χ_{bkg} *in* Ω does not affect the total field, as long as they are changed equally.

However, the fields H_{int} and H_{bkg} critically depend on the chosen values. More specifically, the field generated by the actual *physical* jump of ($\chi_{\text{int}} + \chi_{\text{bkg}}$) at the boundary (which we call *boundary field* later in the article; Fig. 2) is split into a contribution generated by the jump of susceptibility from the interior of the ROI to zero outside the ROI (χ_{int}) and a contribution generated by the jump from zero inside the ROI to the exterior (χ_{bkg}). The former contribution is attributed to the internal field while the latter is attributed to the background field, illustrating the ambiguity of the susceptibility distribution using the traditional definition of internal and background fields. Ideally, the whole boundary field has to be attributed to the background field, H_{bkg}, which is the case only if the value is chosen such that χ_{int} does not undergo a step-change at the boundary, which may not be possible in practical situations, because the susceptibility distribution is not generally constant at the boundary (see Fig. 2).

A.2 Harmonic internal fields equal zero throughout all space

A solution of Eq. (5) in the whole space is globally constant if it is constant outside a bounded set (provided it is smooth enough such that the derivatives exist). If $H_{\text{int}} = \chi_{\text{int}} * d$ is harmonic in Ω ($\nabla^2 H_{\text{int}} = 0$) then χ_{int} satisfies Eq. (5) in Ω. On the other hand, χ_{int} is *by definition* constant outside Ω and on its boundary. Consequently, it follows from the uniqueness of the 2D wave equation that χ_{int} is constant in the whole space and, since a constant susceptibility distribution does not perturb the field, this implies $H_{\text{int}} = 0$ in all space. In other words, harmonic fields generated by susceptibility distributions that satisfy the definition of the internal field are constant zero throughout all space. This finding implies that background field elimination algorithms that eliminate harmonic fields in the ROI cannot remove information about the susceptibility distribution in the ROI.

A.3 Hilbert space projection theorem

The Hilbert projection theorem states that every element x of a Hilbert space has a unique projection $\hat{x}$ onto the closed subspace G, and that this projection is characterized by $\tilde{x} = (x - \hat{x}) \in G^{\perp}$, where $G^{\perp}$ is the orthogonal complement of G. The projection of x onto G, $\hat{x}$, is characterized by the solution of the minimization problem

$$\|\tilde{x}\| = \min_{y \in G} \|x - y\|, \tag{A.1}$$

where $\|\cdot\|$ is the norm generated by the inner product associated with the Hilbert space. In simpler words, the specific element $\hat{x}$ of a given subspace G that has the minimum distance (norm) from x is unique and orthogonal to $\tilde{x}$. Hence, a decomposition of x (e.g. the total field, H) into two components where one of the components is an element of a chosen subspace (e.g. the subspace spanned by all background fields) may be found by solving a projection-type least-squares problem:

$$H_{\text{corr}} = \arg\min_{h} \|H - h\|_2^2 \text{ subject to } \nabla^2 h = 0 \text{ in } \Omega. \tag{A.2}$$

A.4 Formulation of Equation (17) as an unconstrained optimization problem

Equation (17) may be rewritten as an unconstrained problem,

$$\begin{aligned} L_{\min} &= \arg\min_{L} \left(\left\| \left(\underbrace{M' \cdot \nabla^2 H - M' \cdot L}_{A} \right) + L \right\|_2^2 \right) \\ &= \arg\min_{L} \| \underbrace{M' \cdot \nabla^2 H + (1 - M') \cdot L}_{= L'} \|_2^2, \end{aligned} \tag{A.3}$$

where the term on the left-hand side (A) in the objective function (top row) represents the constraint in Eq. (17) and the quantity L' is the Laplacian of the corrected field. The corrected field may be obtained from the solution of Eq. (A.3) by applying the inverse Laplacian to $(M' \cdot \nabla^2 \cdot \vec{H} + (1 - M') \cdot L_{\min})$. Equation (A.3) illustrates that we may understand Eq. (17) as a projection of the masked Laplacian of the total field onto the subspace spanned by all function that are zero inside the ROI (compare with Eq. A.2 in Appendix A.3)—this projection will always be zero.

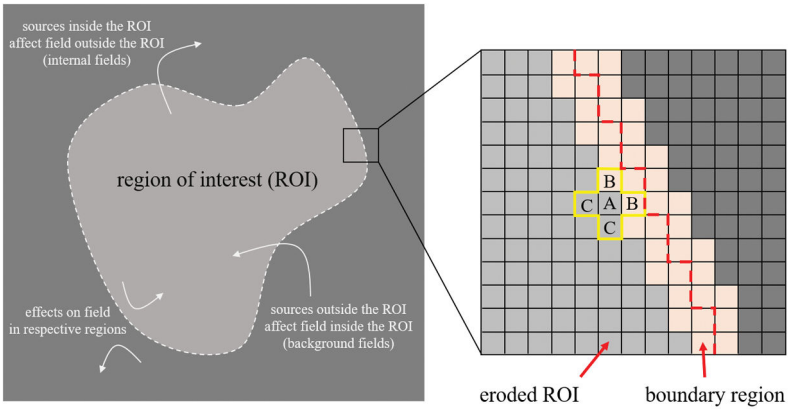

Figure 1.

Schematic illustration of the definition of the ROI (light gray) and the different fields associated to it (white arrows). Sources located within the ROI generate the internal fields, which extends outside the ROI. Sources located outside the ROI generate the background fields, which extend into the ROI. Susceptibility jumps at the boundary generate the boundary field. The enlargement on the right illustrates the boundary region, $\tilde{\Omega}$, (orange) in discretized space. The light gray voxels belong to the eroded ROI. Fields generated by susceptibility changes within the boundary region can neither be regarded as internal nor as external fields. The yellow cross illustrates voxels involved in the calculation of the finite-differences Laplacian for the voxel in the eroded ROI marked with A. Besides voxels in the erode ROI (voxels A and C), the calculation of the Laplacian at voxel A involves voxels in the boundary region (marked with B).

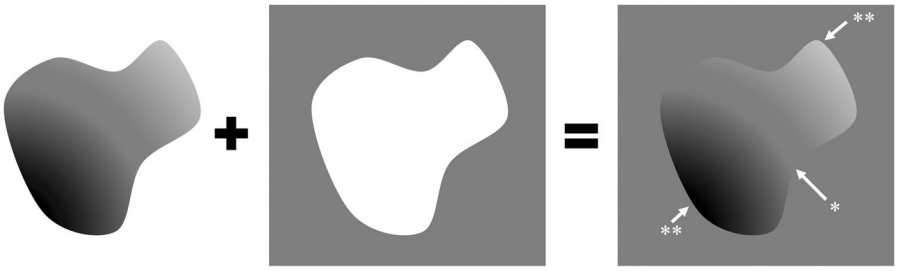

Figure 2.

Schematic illustration of the boundary field. The susceptibility distribution generating the internal field (right) is traditionally understood as having a constant susceptibility value outside the ROI (middle) and susceptibility variations only inside the ROI (left). However, the change of susceptibility at the boundary itself generates fields that depend on the susceptibility jump at the boundary and the overall geometry of the ROI. If the susceptibility difference at the boundary is zero (indicated by *), the boundary does not contribute the boundary field. If the susceptibility difference is different from zero (indicated by **) it can generate boundary fields.

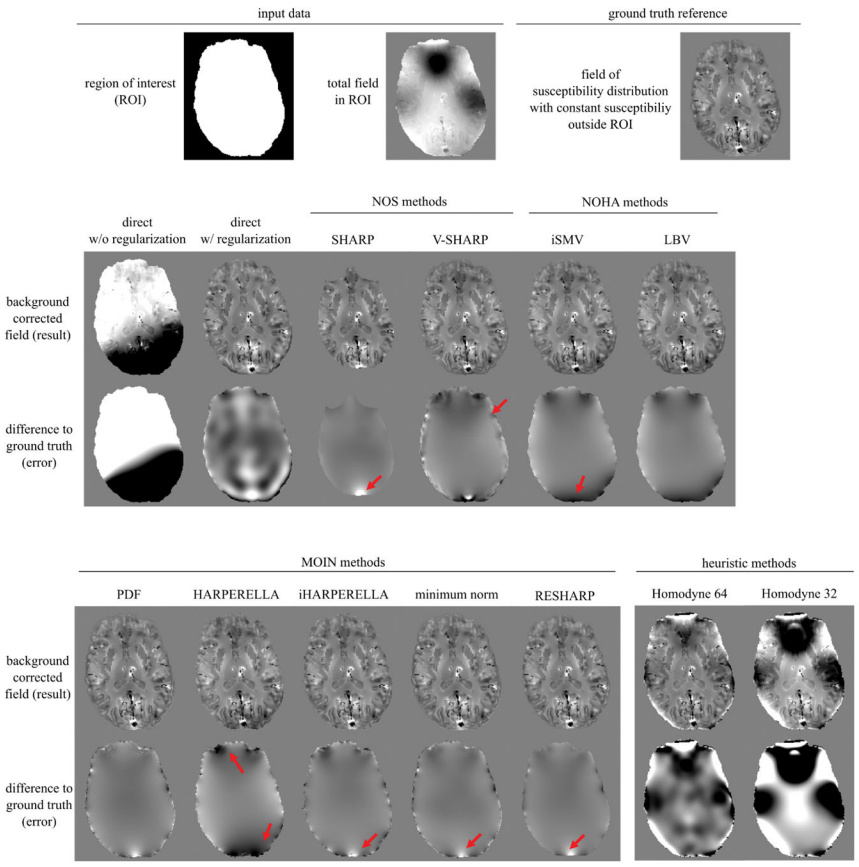

Figure 3.

Comparison of the different background correction strategies discussed in this article. The model and the ROI definition are shown in the top row. The contrast of the background corrected images and the ground truth is −0.8 to 0.8 rad (black to white), that of the difference images is −0.3 to 0.3 rad, and that of the total phase is −3 to 3 rad.

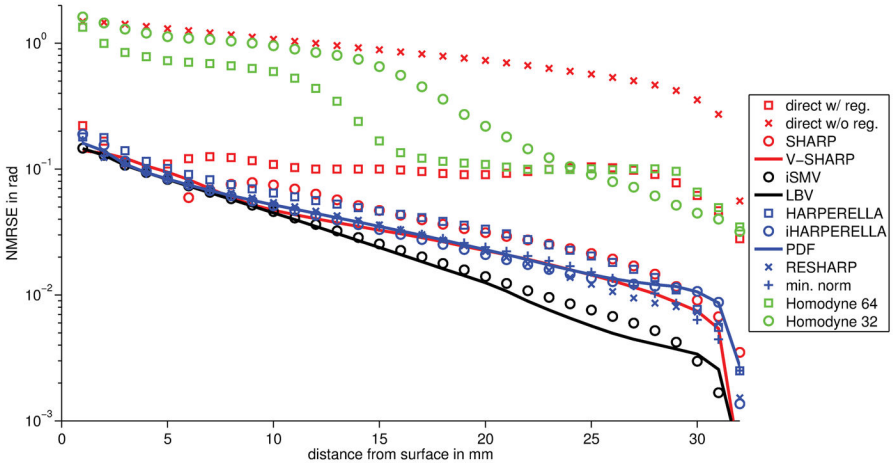

Figure 4.

Quantitative comparison of the different background correction methods. Shown is the NMRSE in a 1 mm thick shell (logarithmic scale) over the distance of the shell from the surface of the brain. The direct solution and NOS methods are plotted in red, NOHA methods are plotted in black, MOIN methods are plotted in blue, and homodyne filtering is plotted in green.

Table 1

Summary of assumptions, limitations and benefits of the background elimination methods reviewed in this article.

Assumptions	Method	Limitations	Benefits
None or limited low frequency content	Direct solution	Artifacts due to finite-differences calculation of the Laplacian at the boundary between eroded ROI and boundary region (see Fig. 1). Suppression of artifacts requires regularization, equivalent to removing low frequency content.	Limited implicit assumptions about field sources. Numerically efficient.
No sources close to boundary (NOS)	SHARP (V-SHARP)	Artifacts due to violation of the assumption close to the boundary. Reduced spatial support with SHARP and inaccurate internal field close to boundaries with V-SHARP. Suppression of artifacts requires regularization.	Robust. Numerically efficient.
No harmonic internal and boundary fields in the boundary region (NOHA)	iSMV	Very slow convergence.	Minimal artifacts in internal field.
	LBV		Minimal artifacts in internal field. Fast convergence.
Minimization of an objective function involving a norm (MOIN)	HARPERELLA	Optimal filter kernel F unknown.	Artifact level similar to NOHA methods.
	iHARPERELLA	Approximate orthogonality leads to residual background fields close to the boundary of the ROI and overfitting of internal field sources close to the boundary. PDF uses only a sub-space of harmonic functions.	Robust techniques. Relatively low artifact level in internal field.
	PDF		
	Minimum norm		
	RESHARP	Regularization introduces artifacts in internal field. Regularization parameter choice determined internal field outcome.	Elimination of unwanted non-harmonic background contributions